

## Optical tomographic reconstruction in a complex head model using *a priori* region boundary information

M Schweiger and S R Arridge

Department of Computer Science, University College London, UK

Received 6 April 1999

**Abstract.** In this paper we investigate the application of anatomical prior information to image reconstruction in optical tomography. We propose a two-stage reconstruction scheme. The first stage is a reconstruction into a low-dimensional region basis, obtained by segmentation of an image obtained by an independent imaging modality, into areas of distinct tissue types. The reconstruction into this basis recovers global averages of the optical tissue parameters of each region.

The recovered distribution of region values provides the starting point for the second stage of the reconstruction into the spatially resolved final image basis. This second step recovers localized perturbations within the regions.

The benefit of this method is the improved stability and faster convergence of the imaging process compared with a direct reconstruction into a spatially resolved basis. This is particularly important for the simultaneous reconstruction of absorption and scattering images, where ambiguities between the two parameters and the resulting problems of crosstalk require a good initial parameter distribution to ensure convergence of the reconstruction.

We use a segmented brain model obtained from a magnetic resonance image as a test case to compare the performance of the two-stage reconstruction and the direct reconstruction from a flat prior, and show that the former achieves superior results in the recovery of localized absorption and scattering hot spots embedded in the background tissue.

(Some figures in this article appear in black and white in the printed version.)

### 1. Introduction

Optical tomography (OT) is a novel imaging modality which seeks to recover the spatial distribution of tissue absorption and scattering parameters in the near-infrared and optical wavelength range from surface measurements of light transmission. While of inherently lower spatial resolution than other imaging methods such as magnetic resonance imaging (MRI) or x-ray computed tomography, OT has the advantage of directly measuring the physiologically relevant tissue and blood oxygenation. OT has therefore a potential as a functional imaging modality, and its applications range from brain oxygenation monitoring in newborn and preterm infants (Wyatt *et al* 1990, Benaron *et al* 1995) to brain activation studies during physical exercise (Maki *et al* 1995) or mental stimulation (Hoshi and Tamura 1993, Gratton *et al* 1995), and breast tumour detection (Fantini *et al* 1996, Zhou *et al* 1997, Moesta *et al* 1998). The reason for the low spatial resolution of OT images is the high scattering coefficient of biological tissue for visible and near-infrared light which makes light propagation an essentially diffuse process. Each detected photon will have undergone multiple scattering events and deviated considerably from the direct line of sight between the source and detector sites, thus blurring the spatial information content it carries. The obtainable image resolution is limited by the width of the photon measurement density function (PMDF), i.e. the area over which a measurement

for a given source–detector pair is sensitive to a change in the optical properties (Arridge 1995, Arridge and Schweiger 1995b).

The scatter-dominated light transport in tissue also makes the reconstruction a nonlinear problem, which prohibits the use of direct reconstruction methods such as the Radon transform. Instead iterative schemes are commonly employed, which use a forward model of light transport to map a given solution of the optical parameters to a set of measurements (Schweiger *et al* 1993, Paulsen and Jiang 1995, Model *et al* 1997, Saquib *et al* 1997). The reconstruction process then becomes a problem of successively modifying the distribution of parameters so as to minimize the difference between measured and modelled data. The high scatter coefficient makes the diffusion equation an adequate forward model for this problem. Its parameters are the absorption coefficient,  $\mu_a(\mathbf{r})$ , diffusion coefficient,  $\kappa(\mathbf{r})$  and refractive index,  $\nu(\mathbf{r})$ . Of these,  $\nu$  is usually considered known, while  $\mu_a$  and  $\kappa$  constitute the solution of the reconstruction problem. Often the transport scattering coefficient  $\mu'_s = (3\kappa)^{-1} - \mu_a$  is used instead of  $\kappa$ . We have previously shown that the problem of reconstructing both parameters simultaneously is ambiguous and can lead to crosstalk artefacts between the absorption and scatter images (Schweiger and Arridge 1999). Both the inherent low resolution and the ill-posedness of the problem make it desirable to combine OT with a second independent imaging modality such as magnetic resonance imaging whose high-resolution spatial information could be used to guide the reconstruction process.

In this paper we investigate the potential of anatomical priors in the simultaneous parameter reconstruction in OT. We propose a reconstruction scheme in two stages. The first stage is a reconstruction into a piecewise constant *region basis*, constructed from the prior. The recovered region values are then used as the starting distribution for the second reconstruction stage into a higher-dimensional regular pixel basis. This second stage recovers parameter variations within the regions such as localized hot spots.

We demonstrate that the availability of a structural prior allows us to recover approximate parameters for the corresponding tissue types, and that a spatial parameter reconstruction starting from the recovered region parameters produces significantly improved images when compared with a reconstruction from a flat prior.

## 2. Incorporating prior information

The idea of incorporating high-resolution structural information as prior knowledge to assist image reconstruction for ill posed inverse problems is a well known concept. The use of anatomical priors obtained from magnetic resonance images in PET and SPECT image reconstruction in a Bayesian framework has been suggested by Chen *et al* (1991) and Gindi *et al* (1993). Leahy and Yan (1991) used an edge prior in the reconstruction of PET images which can be either taken directly from an MRI image, or recovered from the data by a Markov random field model.

We introduced the idea of structural priors into OT in Arridge and Schweiger (1995c, d). In these studies we derived an FEM mesh from a 2D MRI scan, and segmented the image into discontinuous regions, with assigned optical properties. We considered three cases:

*Case 1.* Reconstruction of localized perturbations in absorption given precise knowledge of the background optical properties (absorption and scattering) in each tissue region.

*Case 2.* Reconstruction of a general absorption image given precise knowledge of the background scatter in each region.

*Case 3.* Reconstruction of a general absorption image given incorrect knowledge of the background scatter in each region.

It was found that case 1 and case 2 gave remarkably good quantitative images but that case 3 failed if the assumed scatter was unknown. In the results presented by Arridge and Schweiger (1995c) the case 3 example was quite extreme: we considered uniform scattering as the assumed prior whereas the actual data were generated from regions varying by up to 100% in scattering coefficient. This sensitivity of the reconstructed absorption image to incorrect knowledge of scattering distribution is well known (but often ignored) in OT. As we have advocated, the problem must be considered as a simultaneous reconstruction process. Thus in later studies (Schweiger and Arridge 1997b, Arridge and Schweiger 1998) we have attempted to reconstruct simultaneous images of the complex distribution in head models, given only the outer domain boundary and very approximate information of the scattering and absorption properties in the outermost skin layer. This rather ambitious goal has been only partially met, although one of the most interesting aspects of these studies has been the degree to which the use of alternative transformations of the time-resolved data can lead to marked differences in the quality of the reconstructions (Schweiger and Arridge 1997b).

Some other studies using similar ideas have also been reported. Chang *et al* (1997) reported a similar study to case 1 for breast imaging, and Pogue and Paulsen (1998) reported case 1 and case 2 type images in a simulated model of the rat brain. However, there are several theoretical factors which preclude the realistic development of a combined modality:

- (a) The requirement to know the precise optical properties of tissues, even of only the scatter, is not reasonable.
- (b) The requirement to treat the fully 3D problem is a severe computational burden.
- (c) The presence of non-scattering void regions leads to a breakdown of the assumptions employed in using the diffusion approximation for the underlying model of photon propagation.

In addition there are many practical difficulties in registering MRI pre-scans to the acquisition systems in OT that are outside the scope of this paper.

In this paper we want to address the first of the problems listed above. The issue of void regions, and of 3D reconstruction, is being separately addressed (Firbank *et al* 1996, Schweiger and Arridge 1998, Arridge *et al* 1999). Our proposal can be summarized as follows:

Although MRI scans provide good structural information they cannot be expected to provide optical property information. Therefore although we can identify segmented regions in a MRI scan, we cannot confidently assign optical properties to them. Instead we will use only the region boundary information as prior knowledge.

### 3. Methods

#### 3.1. Forward model

We assume that the data are represented by a nonlinear operator

$$\mathbf{y}^{\mathcal{M}} = F^{\mathcal{M}}[\mu_a, \kappa] \quad (1)$$

where  $\mathcal{M}$  represents a measurement type. We use the diffusion equation as the model of photon transport and a finite-element method (FEM) for its solution in arbitrary geometries. As developed by Arridge *et al* (1993) and Schweiger *et al* (1995), given a domain  $\Omega$ , bounded by  $\partial\Omega$ , the diffusion equation in the FEM framework is expressed, in the frequency domain, as:

$$(\mathbf{K}(\kappa) + \mathbf{C}(\mu) + \zeta \mathbf{A} + i\omega \mathbf{B})\Phi = \mathbf{q}_0 \quad (2)$$

where  $\zeta$  is a constant dependent on the refractive index mismatch at the tissue boundary, and the *system matrices*  $\mathbf{K}$ ,  $\mathbf{C}$ ,  $\mathbf{A}$  and  $\mathbf{B}$  have entries given by

$$K_{ij} = \int_{\Omega} \kappa(\mathbf{r}) \nabla u_i(\mathbf{r}) \cdot \nabla u_j(\mathbf{r}) \, d^n \mathbf{r} \quad (3)$$

$$C_{ij} = \int_{\Omega} \mu_a(\mathbf{r}) u_i(\mathbf{r}) u_j(\mathbf{r}) \, d^n \mathbf{r} \quad (4)$$

$$B_{ij} = \frac{1}{c} \int_{\Omega} u_i(\mathbf{r}) u_j(\mathbf{r}) \, d^n \mathbf{r} \quad (5)$$

$$A_{ij} = \int_{\partial\Omega} u_i(\mathbf{r}) u_j(\mathbf{r}) \, d^{n-1} S \quad (6)$$

where  $u_i$  is the shape function associated with node  $i$  of the FEM mesh. Equation (2) is formally solved by matrix inversion

$$\hat{\Phi} = (\mathbf{K}(\kappa) + \mathbf{C}(\mu) + \zeta \mathbf{A} + i\omega \mathbf{B})^{-1} \mathbf{q}_0 = \hat{\mathbf{G}}(\omega) \mathbf{q}_0 \quad (7)$$

where  $\hat{\mathbf{G}}(\omega)$  is the discrete representation of the Green operator  $\hat{\mathcal{G}}$ .

Standard direct or iterative methods like Cholesky factorization (Arridge *et al* 1993) or biconjugate gradients in the complex case (Schweiger and Arridge 1997a) can be employed to solve equation (7). In large problems, such as occur in 3D, the sparse nature of the matrices  $\mathbf{K}$ ,  $\mathbf{C}$ ,  $\mathbf{A}$ ,  $\mathbf{B}$  can be utilized by a sparse storage scheme in combination of sparse versions of the Cholesky and conjugate gradient solvers (Schweiger and Arridge 1998).

The modelled data are obtained by application of a measurement operator

$$\mathbf{y}^M = \mathcal{M}[\Phi] = \mathcal{M}[\hat{\mathbf{G}}(\omega) \mathbf{q}_0]. \quad (8)$$

Our approach has been to use measurement operators of *normalized integral transform* type, that can be efficiently calculated directly from the form (2) without explicitly solving the parabolic time-domain version of the equation (Arridge and Schweiger 1995a, Schweiger and Arridge 1997c). This approach reduces the cost of the forward model by an order of magnitude. In this paper we use the skew ( $c_3$ ) and Laplace transform ( $L(s)$ ) as the forward data from which to reconstruct. This combination has previously been shown to provide the best results for simultaneous parameter reconstructions (Schweiger and Arridge 1997b).

### 3.2. Basis expansion

We assume that  $\mu_a(\mathbf{r})$  and  $\kappa(\mathbf{r})$  are expressed in a basis

$$\kappa(\mathbf{r}) = \sum_{k=1}^{R_\kappa} \kappa_k v_k^{(\kappa)}(\mathbf{r}) \quad \mu_a(\mathbf{r}) = \sum_{k=1}^{R_\mu} \mu_{a_k} v_k^{(\mu)}(\mathbf{r}). \quad (9)$$

Using this basis expansion of  $(\kappa(\mathbf{r}), \mu_a(\mathbf{r}))$  we can further express  $\mathbf{K}$  and  $\mathbf{C}$  as:

$$\begin{aligned} \mathbf{K}(\kappa) &= \sum_k^{R_\kappa} \kappa_k \mathbf{V}_k(\kappa) \\ \mathbf{C}(\mu_a) &= \sum_k^{R_{\mu_a}} \mu_{a_k} \mathbf{V}_k(\mu_a) \end{aligned} \quad (10)$$

where  $\mathbf{V}_k(\kappa)$ ,  $\mathbf{V}_k(\mu_a)$  represent *basis system matrices* whose entries are given by

$$\mathbf{V}_{k,ij}(\kappa) = \int_{\Omega} v_k^{(\kappa)}(\mathbf{r}) \nabla u_i(\mathbf{r}) \cdot \nabla u_j(\mathbf{r}) \, d^n \mathbf{r} \quad (11)$$

$$\mathbf{V}_{k,ij}(\mu_a) = \int_{\Omega} v_k^{(\mu)}(\mathbf{r}) u_i(\mathbf{r}) u_j(\mathbf{r}) \, d^n \mathbf{r}. \quad (12)$$

A number of different strategies for defining reconstruction bases are possible.

- (a) A natural choice is to use the mesh structure given by the FEM forward model, i.e.

$$v_k^{(\kappa, \mu_a)}(\mathbf{r}) = u_k(\mathbf{r}). \tag{13}$$

However the mesh resolution for the FEM solver is governed by considerations of the numerical stability of the solver, not by the resolution of the reconstructed image. This leads to an unnecessarily high-dimensional basis, and may require severe filtering and regularization to ensure convergence of the inverse problem.

- (b) A second independent mesh of lower resolution may be used (Paulsen *et al* 1995). The mesh density can be adapted to the expected image resolution, and may be spatially variable.
- (c) A regular pixel grid has been suggested (Schweiger *et al* 1993), which in 2D is given by basis functions

$$v_k^{(\kappa, \mu_a)}(x, y) = \begin{cases} \max\left(1 - \frac{|x - x_k|}{s_x}, 0\right) \max\left(1 - \frac{|y - y_k|}{s_y}, 0\right) & \text{if } (x, y) \in \Omega \\ 0 & \text{otherwise} \end{cases} \tag{14}$$

where  $(x_k, y_k)$  is the centre of pixel  $k$  and  $s_x$  and  $s_y$  are the grid spacings in  $x$  and  $y$  directions (see figure 1). Support is truncated outside  $\Omega$ .

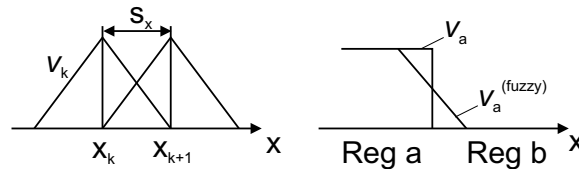


Figure 1. Schematic basis function for regular pixel grid (left) and at region boundary (right).

- (d) A piecewise constant *region basis* derived from anatomical prior information, whereby  $\Omega$  is divided into non-overlapping regions,  $\Omega = \bigcup_k \Omega_k$ . The basis is then given by

$$v_k^{(\kappa, \mu_a)}(\mathbf{r}) = \begin{cases} 1 & \text{if } \mathbf{r} \in \Omega_k \\ 0 & \text{otherwise.} \end{cases} \tag{15}$$

A variant of this method is a *fuzzy region basis* which replaces the sharp step of equation (15) by a transition zone of finite width at region boundaries. A fuzzy basis may be applicable for regions without well defined boundaries such as the grey/white matter interface, or when the anatomical prior is imperfect.

### 3.3. Problem derivative

The problem of image reconstruction is to determine the spatial distribution of optical parameters  $\mu_a(\mathbf{r})$  and  $\kappa(\mathbf{r})$  which minimizes an objective function based on the difference of data. We have developed a number of iterative approaches, including Levenberg–Marquadt schemes and nonlinear conjugate gradients. These have been discussed in detail by Arridge and Schweiger (1999) and Arridge (1999).

All inverse solver schemes implicitly require the derivative  $\partial y_{sm}^M / \partial x_k$  of each measurement  $m$  from each source  $s$  with respect to each basis coefficient  $k$ , with  $x$  representing either  $\mu_a$  or  $\kappa$ .

As described by Arridge and Schweiger (1999) and Arridge (1999), for linear measurement operators, this may be expressed either in *direct form*

$$\frac{\partial y_{sm}^{\mathcal{M}}}{\partial x_k} = \mathcal{M}(m) \left[ \frac{\partial \Phi_s}{\partial x_k} \right] = -\mathcal{M}(m) [\hat{\mathbf{G}} \mathbf{V}_k(x) \Phi_s] \quad (16)$$

or in *adjoint form*

$$\frac{\partial y_{sm}^{\mathcal{M}}}{\partial x_k} = \mathcal{M}(m) \left[ \frac{\partial \Phi_s}{\partial x_k} \right] = -\mathcal{M}[\Psi_m^T \mathbf{V}_k(x) \Phi_s] \quad (17)$$

where  $\Psi_m$  is the solution to the adjoint problem

$$(\mathbf{K}(\kappa) + \mathbf{C}(\mu) + \zeta \mathbf{A} - i\omega \mathbf{B}) \Psi_m = \mathbf{q}_m^+ \quad (18)$$

where  $\mathbf{q}_m^+$  is an *adjoint source*, initializing the boundary nodes of the element containing the  $m$ th measurement. For the non-linear measurement operators used in our approach the derivative expressions are more complex, but can still be expressed in either direct or adjoint form. For details we refer to Arridge and Schweiger (1999) and Arridge (1999).

### 3.4. A two-stage reconstruction algorithm

Because of the difficulties described in section 2 of reconstructing general distributions of scattering and absorption parameters, we propose a two-stage algorithm:

*Stage 1.* Reconstruction of average tissue parameters in segmented regions.

*Stage 2.* Full reconstruction into a local basis using the region values recovered in stage 1.

In stage 1, we use the region basis and the direct form of the derivative given in (16) to construct a Jacobian matrix of the form

$$\mathbf{J} \triangleq \begin{bmatrix} \frac{\partial y^{\mathcal{M}_1}}{\partial \mu_1} & \frac{\partial y^{\mathcal{M}_1}}{\partial \mu_2} & \cdots & \frac{\partial y^{\mathcal{M}_1}}{\partial \mu_R} & \frac{\partial y^{\mathcal{M}_1}}{\partial \kappa_1} & \frac{\partial y^{\mathcal{M}_1}}{\partial \kappa_2} & \cdots & \frac{\partial y^{\mathcal{M}_1}}{\partial \kappa_R} \\ \frac{\partial y^{\mathcal{M}_2}}{\partial \mu_1} & \frac{\partial y^{\mathcal{M}_2}}{\partial \mu_2} & \cdots & \frac{\partial y^{\mathcal{M}_2}}{\partial \mu_R} & \frac{\partial y^{\mathcal{M}_2}}{\partial \kappa_1} & \frac{\partial y^{\mathcal{M}_2}}{\partial \kappa_2} & \cdots & \frac{\partial y^{\mathcal{M}_2}}{\partial \kappa_R} \\ \vdots & \vdots & \vdots & \vdots & \vdots & \vdots & \vdots & \vdots \\ \frac{\partial y^{\mathcal{M}_T}}{\partial \mu_1} & \frac{\partial y^{\mathcal{M}_T}}{\partial \mu_2} & \cdots & \frac{\partial y^{\mathcal{M}_T}}{\partial \mu_R} & \frac{\partial y^{\mathcal{M}_T}}{\partial \kappa_1} & \frac{\partial y^{\mathcal{M}_T}}{\partial \kappa_2} & \cdots & \frac{\partial y^{\mathcal{M}_T}}{\partial \kappa_R} \end{bmatrix} \quad (19)$$

where  $\{\mu_k; k = 1 \dots R_\mu\}$ ,  $\{\kappa_k; k = 1 \dots R_\kappa\}$  enumerate the region values for absorption and diffusion coefficient, and  $\{\mathcal{M}_t; t = 1, \dots, T\}$  enumerate the measurement types. For the results presented in this paper we consider four regions: skin, bone, grey matter and white matter, and two measurement types: skew ( $c_3$ ) and Laplace transform data ( $L(s)$ ), which are those we have advocated as optimal for simultaneous reconstructions (Schweiger and Arridge 1997b). Thus the first stage reconstruction is an optimization over only eight variables, and is conveniently solved using a Levenberg–Marquardt approach, wherein we repeatedly solve

$$\mathbf{h} = (\mathbf{J}^T \mathbf{J} + \lambda \mathbf{I})^{-1} \mathbf{J}^T \mathbf{b} \quad (20)$$

where

$$\mathbf{b} = \begin{bmatrix} \mathbf{y}^{\mathcal{M}_1} - F^{\mathcal{M}_1}[\mu_a, \kappa] \\ \mathbf{y}^{\mathcal{M}_2} - F^{\mathcal{M}_2}[\mu_a, \kappa] \\ \vdots \\ \mathbf{y}^{\mathcal{M}_T} - F^{\mathcal{M}_T}[\mu_a, \kappa] \end{bmatrix} \quad \mathbf{h} = \begin{bmatrix} \Delta \mu_{\text{skin}} \\ \Delta \mu_{\text{bone}} \\ \Delta \mu_{\text{GM}} \\ \Delta \mu_{\text{WM}} \\ \Delta \kappa_{\text{skin}} \\ \Delta \kappa_{\text{bone}} \\ \Delta \kappa_{\text{GM}} \\ \Delta \kappa_{\text{WM}} \end{bmatrix}. \quad (21)$$

The reconstruction into a region basis gives global region parameters, but it will not recover localized hot spots within a region. It is therefore followed by a second reconstruction stage into a higher-dimensional basis, starting from the recovered region values. In this paper we use a bilinear pixel basis for this second step. The high dimensionality of this basis makes the application of the Levenberg–Marquardt method to the second stage impractical, because it requires the explicit calculation of  $\mathbf{J}$ . Instead we use a nonlinear conjugate gradient method which minimizes an objective function whose gradient is calculated by an adjoint scheme, as reported by Arridge and Schweiger (1998). A gradient-based reconstruction method applied to a finite-difference forward model has recently been reported by Hielscher *et al* (1999).

The second stage of the reconstruction uses the result of the initial region reconstruction as its initial guess for the distribution of optical parameters. The combined two-stage algorithm can therefore be considered as simultaneous reconstruction without detailed knowledge of optical parameter distributions in normal tissue.

#### 4. Model head generation

We demonstrate the effect of anatomical priors on the simultaneous reconstruction of absorption and scatter by means of a two-dimensional head model. To obtain the target image and data, the following steps are performed:

*Layered head model.* Since we are using only an approximation to a real physical model, we could propose a ‘generic model’ of, for example, concentric circles (Okada *et al* 1997). However, to illustrate a step towards the use of a combined MRI/OT modality, we use an MRI image (figure 2) segmented into four regions of skin, bone, grey and white matter, by means of a standard image processing tool, to generate more complex region outlines. Five additional small objects are added in the grey and white matter regions, to simulate localized perturbations. The result of the segmentation process is shown in figure 3.

*Forward mesh generation.* The outermost segment (the outer skin surface) is applied to an adaptive mesh generator to create the mesh for the FEM solver. The resulting mesh, shown in figure 4 (left), contains  $N = 10\,952$  nodes and  $D = 21\,555$  triangles. Each node receives a label to denote the region it belongs to, given the above segmentation. Optical properties are then

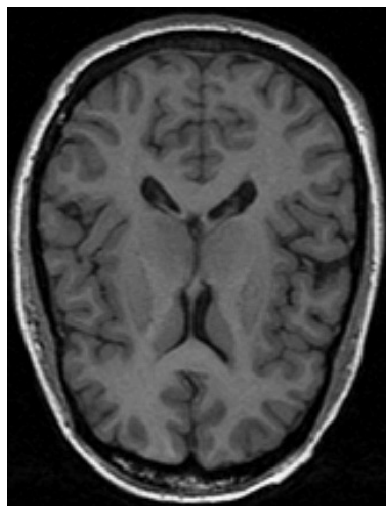
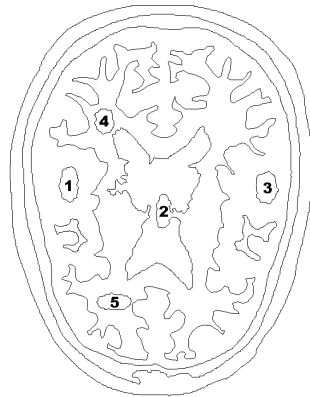
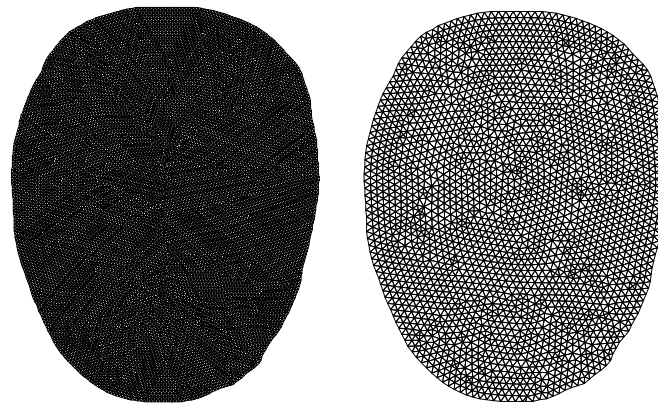


Figure 2. Magnetic resonance image of a head ( $352 \times 472$  pixels) used for mesh generation.



**Figure 3.** Result of the segmentation of figure 2 into skin, skull, grey and white matter. In addition, outlines of five small perturbations in the grey and white matter regions have been created to simulate lesions. Perturbations 1–3 have increased  $\mu_a$  values, perturbations 4 and 5 increased  $\mu'_s$  values.



**Figure 4.** Meshes used by the finite element solver. Left: high-resolution mesh for forward data generation (10952 nodes, 21555 triangles), right: low-resolution mesh used by the forward model within the inverse solver (2476 nodes, 4788 triangles).

assigned to each of the four background regions according to literature values (van der Zee 1993, Firbank *et al* 1993). The values for the background regions and the five localized perturbations are listed in table 1. The resulting distributions of absorption and scattering are shown in figure 5. The mesh is scaled to a sagittal diameter of 80 mm typical for the size of a preterm infant.

*Application of fuzzy basis.* To account for gradual transitions between region values, in particular at the interface between grey and white matter, a mean filter is applied to the nodal parameter distribution  $\mathbf{x} = \{x_i; i = 1, \dots, N\}$ :

$$\tilde{x}_i = \frac{1}{\text{nn}(i) + 1} \left( x_i + \sum_{j=1}^{\text{nn}(i)} x_{\text{n}(i,j)} \right) \quad (22)$$

where  $\text{nn}(i)$  is the number of neighbouring nodes of node  $i$ , and  $\text{n}(i, j)$  is the  $j$ th neighbour of  $i$ . We apply filter (22) iteratively five times to the forward mesh to obtain the final target absorption and scatter images, shown in figure 6.

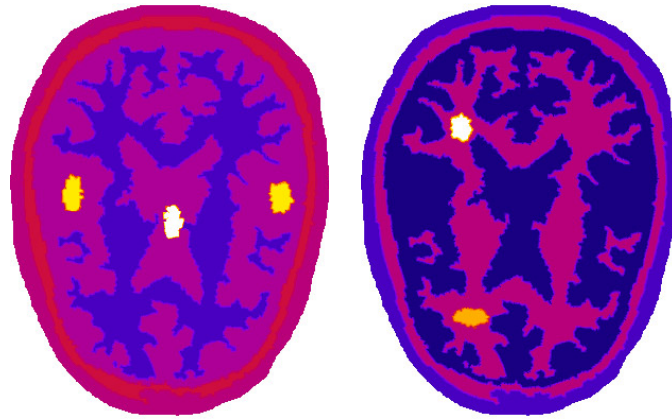


**Figure 5.** Parameter distribution of absorption (left) and scatter (right) with embedded perturbations in the target mesh before application of fuzzy basis.

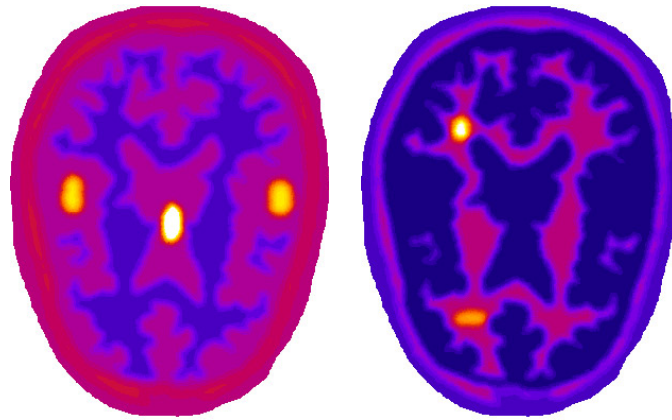


**Figure 6.** Final fuzzy target parameter distributions used to generate forward data.

*Data generation.* 32 source and 32 detector locations at equal angular spacing as measured from the mesh centre are defined along the mesh boundary. In the FEM solver the sources are modelled as isotropic point sources at a depth of  $1/\mu'_s = 1.0$  mm below the surface, to simulate a collimated pencil beam normally incident on the surface (Schweiger *et al* 1993). Skew ( $c_3$ ) and Laplace transform data ( $L(s = 0.001 \text{ ps}^{-1})$ ) (ps = picoseconds) are generated for each of the 1024 source–detector combinations.

*Noise.* The simulated data are contaminated with Gaussian-distributed random noise, with a standard deviation given by the noise model presented by Arridge *et al* (1995) assuming  $10^4$  photons collected at each detector.

## 5. Reconstruction results

We want to demonstrate the influence of various levels of prior information on the ability to simultaneously reconstruct absorption and scatter images from the generated data. The following sets of reconstructions are performed:

**Table 1.** Optical parameters for the four background tissue types and the perturbations in the target images.

Tissue type	$\mu_a$ [mm <sup>-1</sup> ]	$\mu'_s$ [mm <sup>-1</sup> ]
background tissue		
skin	0.022	1.0
skull	0.025	2.0
grey matter	0.02	0.55
white matter	0.01	2.0
perturbations		
1	0.05 (g.m. $\times$ 2.5)	0.55 (g.m.)
2	0.1 (g.m. $\times$ 5)	0.55 (g.m.)
3	0.05 (g.m. $\times$ 2.5)	0.55 (g.m.)
4	0.01 (w.m.)	6 (w.m. $\times$ 3)
5	0.01 (w.m.)	4 (w.m. $\times$ 2)

**Table 2.** List of test reconstructions. In all cases the reconstruction basis is a  $32 \times 32$  pixel basis. Recovered background values are obtained from region reconstructions.

Case	Parameters	From background	Excluding
RECON1	$\mu_a$ only	correct	—
RECON2	both	correct	—
RECON3	both	correct	skin, skull
RECON4	both	correct	skin, skull, white m.
RECON5	$\mu_a$ only	recovered	—
RECON6	both	recovered	—
RECON7	both	recovered	skin, skull
RECON8	both	recovered	skin, skull, white m.
RECON9	both	homog.	—

- (a) *Reconstruction into  $32 \times 32$  pixel basis from homogeneous background.* This assumes no structural information and no knowledge of background parameters.
- (b) *Reconstruction into pixel basis from correct background.* In this case we assume knowledge of the region boundaries *and* the optical parameters of the background within each region. The reconstruction problem is therefore the recovery of the localized high-contrast object embedded in the grey and white matter regions.
- (c) *Two-stage, region and pixel basis.* In this case we assume knowledge of the region boundaries, but start with a reconstruction into the regions from a homogeneous background. From the recovered region values, a reconstruction into a pixel basis is performed as before.

In addition, we investigate the effect of reconstructing only regions of interest, by keeping pixels within particular regions fixed at their initial values (or the values recovered in stage 1 of the algorithm). By this method it is possible to reduce the complexity of the reconstruction, by excluding regions whose parameter distributions are known with sufficient accuracy, or are not of interest in the image. Table 2 lists the parameters of the reconstructions performed. The reconstruction basis in all cases is a  $32 \times 32$  pixel basis, and a nonlinear conjugate gradient solver is employed. The mesh used by the FEM forward solver in the reconstruction, shown in figure 4 (right), has a lower resolution than the mesh employed for data generation. No regularization terms were used in these tests, but a median filter was applied to the pixel basis, at each iteration of the algorithm (Schweiger *et al* 1993).

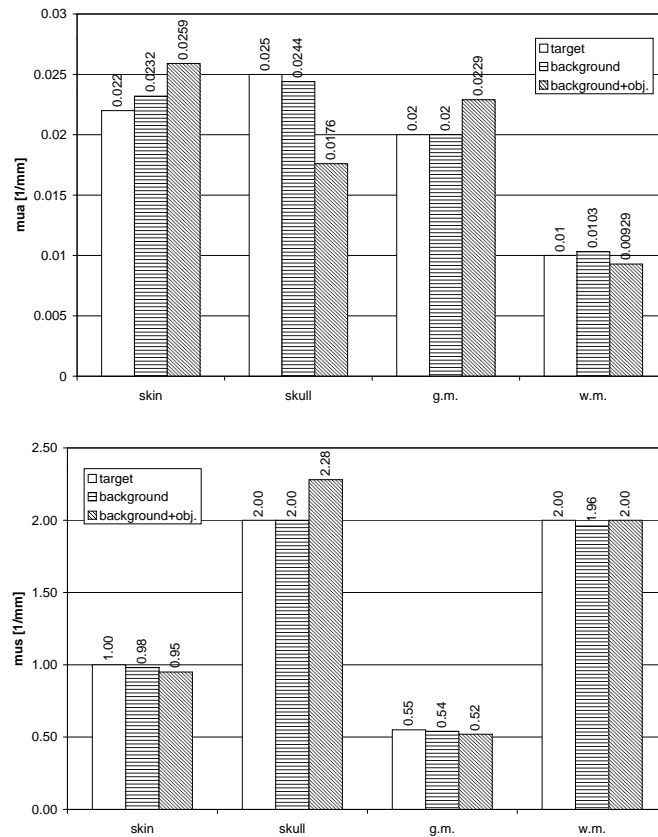


**Figure 7.** Results of reconstruction into four regions using data obtained from background images and from background images with embedded objects. Top: absorption, bottom: scatter parameters.

The background parameters required by RECON5–8 are obtained by a two-parameter region reconstruction into a four-region basis, assuming a perfect structural prior for the background regions, but no knowledge of the hot spots. During the reconstruction the region basis is assumed piecewise constant, as given by (15), but to obtain the starting distribution for the second stage of the reconstruction, the filter defined in equation (22) is applied to generate a fuzzy region basis.

The starting parameter distribution for the region reconstruction is homogeneous, with  $\mu_a = 0.022 \text{ mm}^{-1}$  and  $\mu'_s = 1 \text{ mm}^{-1}$  corresponding to skin values. (Note that we give results of the second parameter in terms of  $\mu'_s$  because it is more commonly used in the OT community than  $\kappa$ .) Reconstruction results after convergence of the Levenberg–Marquadt solver are shown in figure 7. For comparison we also show the results of a region reconstruction without the presence of the hot spots. In this latter case excellent recovery of the region background values can be achieved. The residual errors are caused by data noise and the fact that the region boundaries cannot be exactly matched in the forward and inverse models, because they use meshes of different resolution. The fact that this mismatch does not prevent the region reconstruction from converging towards the correct solution is encouraging, showing that no high precision knowledge of the region boundaries may be required.

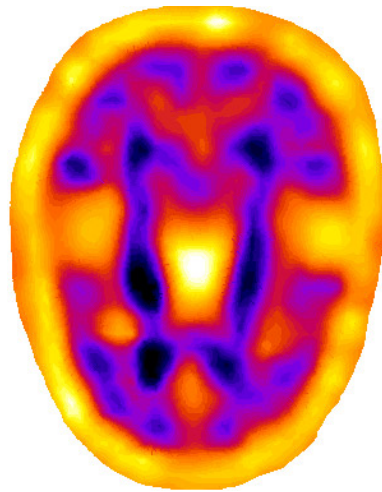


**Figure 8.** RECON1: reconstruction of  $\mu_a$  only from correct background values of  $\mu_a$  and  $\mu'_s$ .

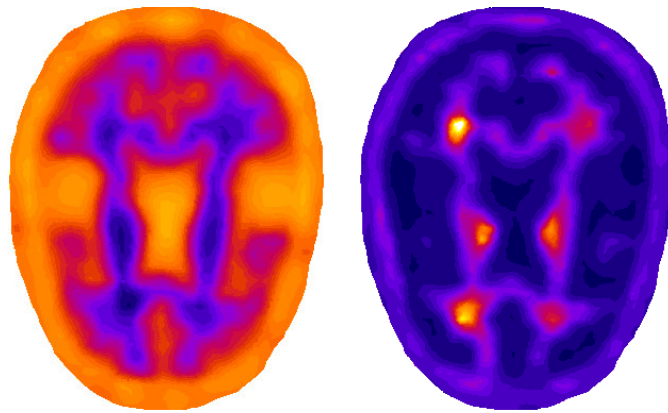


**Figure 9.** RECON2: reconstruction of both parameters from correct background values (left,  $\mu_a$ ; right,  $\mu'_s$ ).

In the presence of perturbations we obtain larger deviations from the correct values. Interestingly the largest error occurs in the skull region although there are no perturbations present in this region. Conversely, the grey and white matter compartments, which do contain perturbations, show a remarkable agreement with the correct background values. A possible explanation for this effect is that reconstruction artefacts tend to be shifted towards the mesh boundary as the magnitude of the photon measurement density functions increases towards the source and detector locations at the surface (Arridge and Schweiger 1995b).

The results of the reconstructions for cases RECON1–9, after the conjugate gradient solver has run to convergence, are shown in figures 8–16.

In each case, absorption is shown in the left image, scatter (where applicable) in the right image. We find that the reconstructions from both correct and recovered background values (RECON1–4 and RECON5–8, respectively) are superior to that from a homogeneous background (RECON9). While the latter recovers some of the background structure, the hot spots remain weak, with the exception of the lower scatter perturbation. In contrast, the

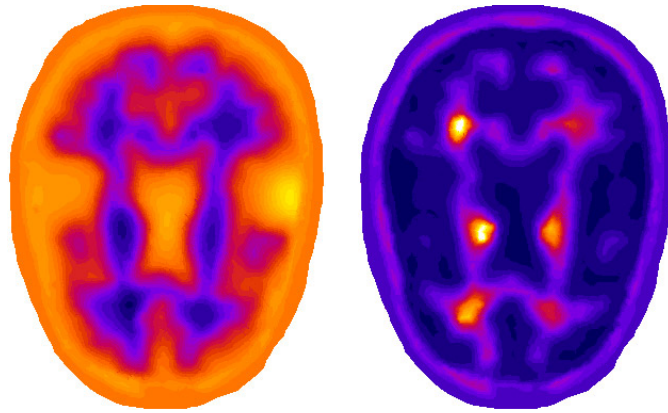


**Figure 10.** RECON3: reconstruction of both parameters from correct background values, holding skin and skull regions fixed.

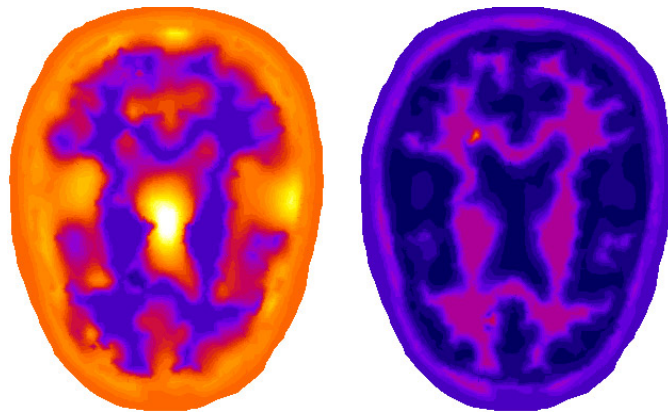


**Figure 11.** RECON4: as figure 10, but in addition holding white matter region fixed.

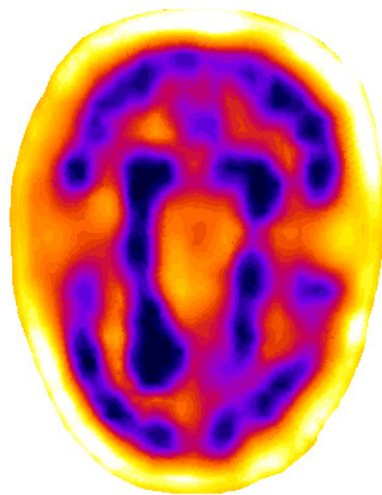


**Figure 12.** RECON5: reconstruction of  $\mu_a$  only from recovered background values of  $\mu_a$  and  $\mu'_s$ .

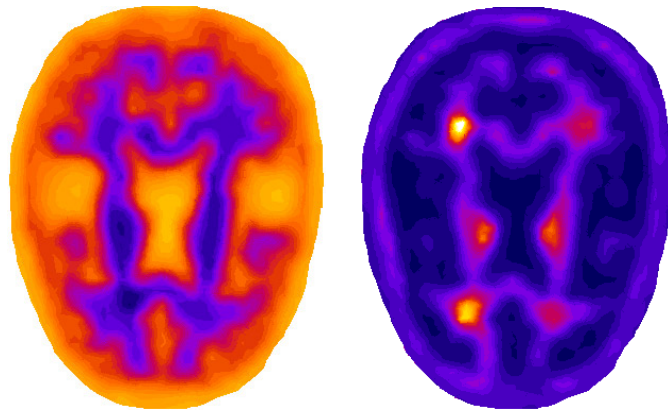


**Figure 13.** RECON6: reconstruction of both parameters from recovered background values.

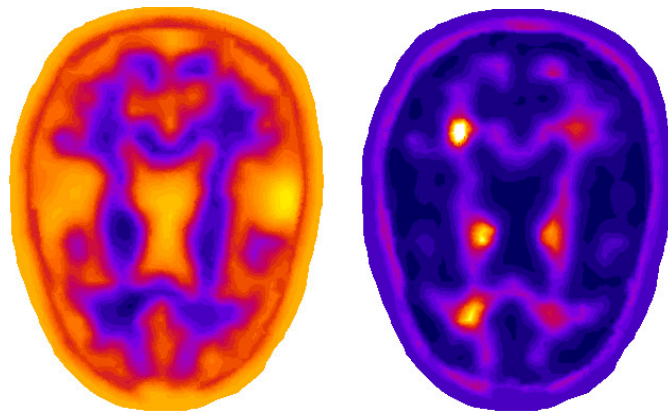


**Figure 14.** RECON7: as figure 13, but holding skin and skull regions fixed.

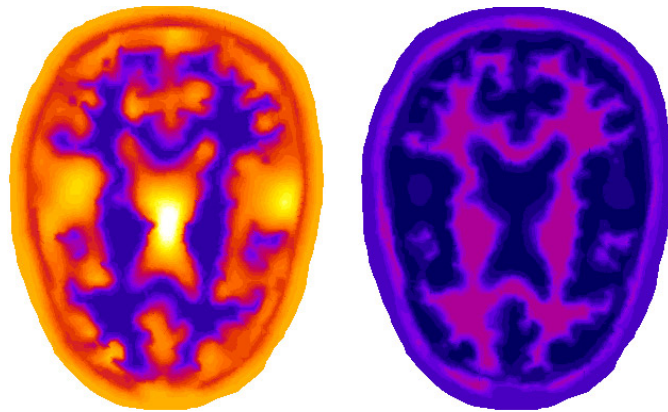


**Figure 15.** RECON8: as figure 14, but in addition holding white matter region fixed.

reconstruction from recovered background values (RECON6, see figure 13) recovers both scatter perturbations, and has more pronounced absorption features, without the boundary artefacts present in RECON9.

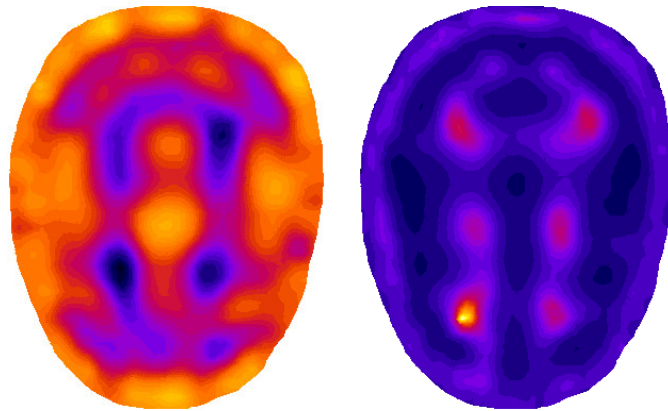


**Figure 16.** RECON9: direct reconstruction of both parameters from homogeneous background values.

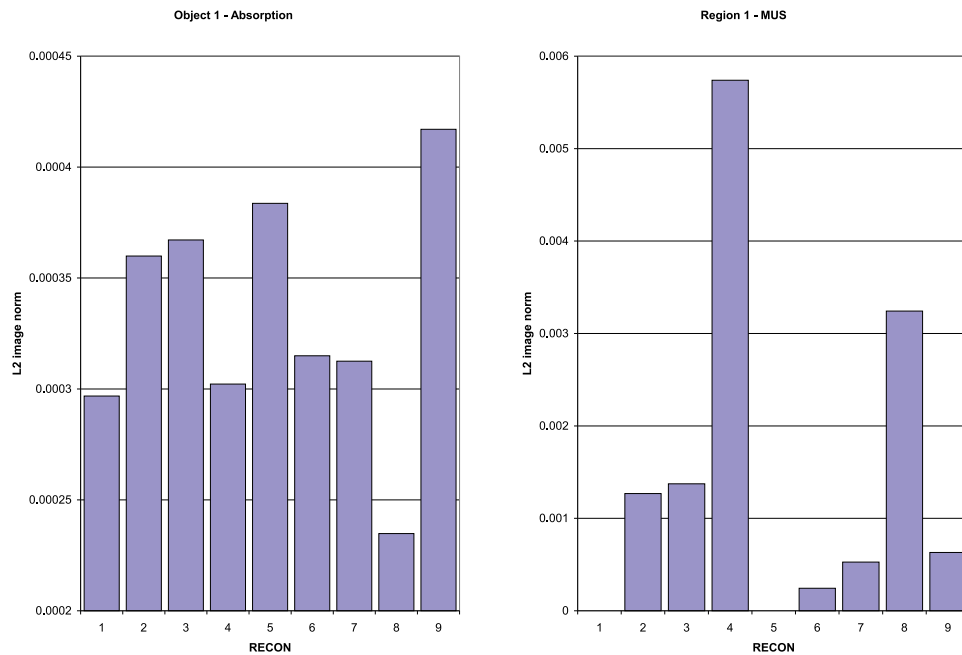


**Figure 17.**  $L_2$  error norm of  $\mu_a$  images (left graph) and  $\mu'_s$  images (right graph) for the left absorption hot spot (object 1), for reconstructions from correct background (RECON 1–4), and reconstructions from recovered background (RECON 5–8). RECON9 (direct reconstruction from homogeneous background) is included as reference.

Excluding regions from the reconstruction can lead to improvement when starting from correct background values. See for example the absorption image of RECON4 (figure 11)—note that the scatter hot spots cannot be recovered in this case because the white matter region is fixed.

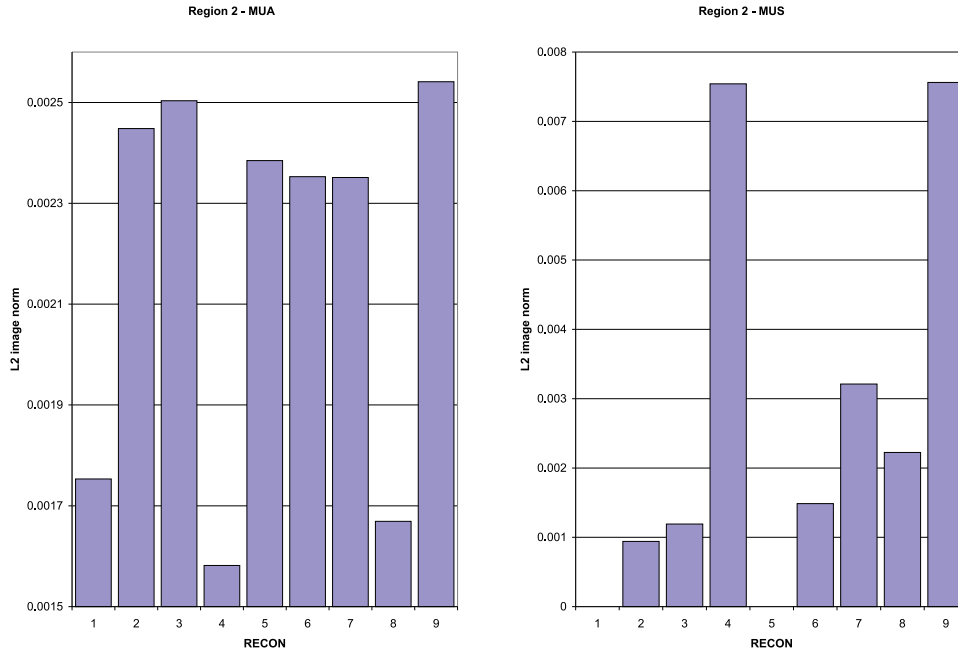


**Figure 18.**  $L_2$  error norm of  $\mu_a$  images (left graph) and  $\mu'_s$  images (right graph) for the central absorption hot spot (object 2).

In the reconstructions from recovered background values the effect of keeping regions fixed is less positive. In particular RECON7, where skin and skull regions are fixed, produces worse results than RECON6. This can be attributed to the large deviation of the recovered values in these regions from the correct parameters, resulting in artefacts in the remaining regions.

This effect is even more striking for the single-parameter reconstructions (RECON1 and 5) where the  $\mu'_s$  distribution is held fixed at the correct and recovered background values, respectively. While a good result is obtained in the reconstruction from correct background (figure 8), the reconstruction from recovered region values is very poor, completely failing to recover any of the hot spots (figure 12). This demonstrates that a successful single-parameter reconstruction requires not only approximate but perfect knowledge of the second parameter, which is generally not available in clinical applications.

For a quantitative assessment of the recovery of the hot spots we compute the  $L_2$  image norms of the absorption and scatter images, integrated over the area  $\Omega_p$  covered by a given perturbation  $p$ :

$$\varepsilon_x^{(p)} = \int_{\Omega_p} |x(\mathbf{r})^{\text{recon}} - x(\mathbf{r})^{\text{target}}|^2 d^n \mathbf{r}. \quad (23)$$

Figures 17–19 show  $\varepsilon_{\mu_a}$  and  $\varepsilon_{\mu'_s}$  for perturbations 1, 2 and 4, respectively, for all reconstructions. The missing entries in the  $\varepsilon'_{\mu_s}$  graphs (RECON1 and 5) refer to the  $\mu_a$ -only reconstructions. The following observations can be made:

- Reconstruction of the grey matter region alone (RECON4 and 8) leads to improvements in the recovery of perturbation  $\mu_a$  values, but seriously corrupts the  $\mu'_s$  values. Note that object 4 (figure 19) is in the white matter region and thus kept fixed in RECON4 and 8 so that the values shown there are simply due to the background values initially assigned.

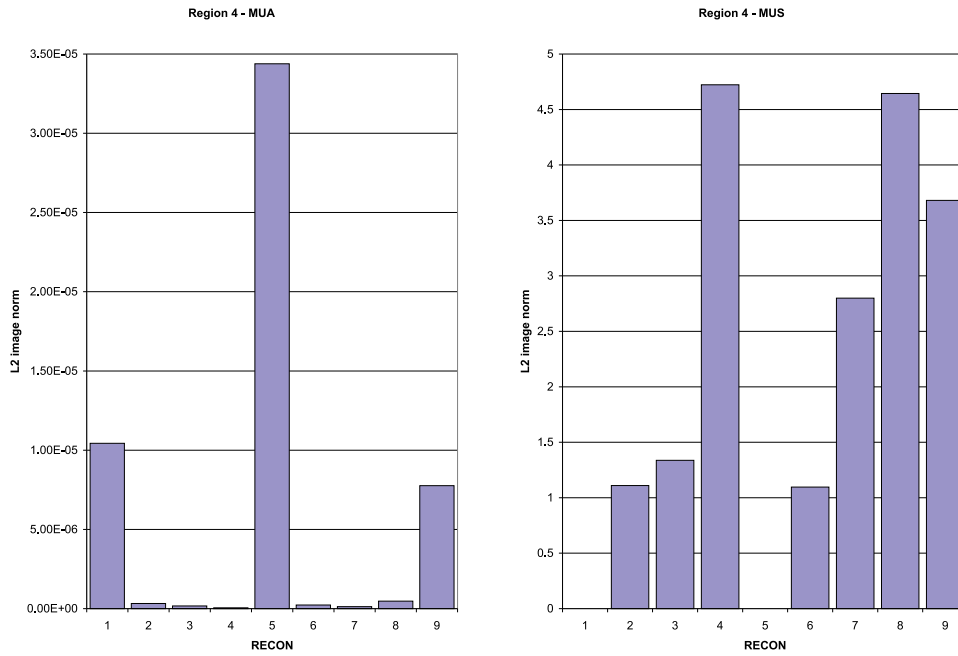


**Figure 19.** L<sub>2</sub> error norm of  $\mu_a$  images (left graph) and  $\mu_s'$  images (right graph) for the top scatter hot spot (object 4).

- The reconstruction of  $\mu_a$  only shows good results for objects 1 and 2 when starting from correct background parameters (RECON1), but is inferior to a simultaneous reconstruction when starting from recovered background parameters (RECON5). The reconstructed absorption value of the scatter perturbation (object 4) is dramatically degraded in the  $\mu_a$  only reconstructions, indicating a strong cross-talk artefact.
- Most relevant for the assessment of the benefit of region priors is the comparison between RECON6 (reconstruction from recovered region values) and RECON9 (reconstruction from flat prior). We find that the former produces superior results in all cases.

## 6. Conclusion

The need in OT to reconstruct the absorption and scatter distribution of an object simultaneously poses a fundamental difficulty, and often results in artefacts caused by cross-talk between the parameters. It is therefore useful to incorporate any prior information available into the reconstruction process.

We have discussed the application of anatomical boundary information as a prior. We have introduced the idea of a two-step algorithm wherein the optical properties in regions are first reconstructed, before proceeding to a general reconstruction into the full basis of the image. We have tested this method by reconstructing a 2D head model from data generated by a FEM forward model. The model, whilst simplistic due to the 2D geometry and omission of void regions, nonetheless shows a significant improvement of the quantitative accuracy of the reconstruction when the region prior is used.

We have further shown that the reconstruction of a single parameter, or the reconstruction of only some of the regions is degraded if the omitted parameters or regions are only approximately known. Since in practical applications complete *a priori* knowledge of parameter values will not be available, the simultaneous reconstruction of both parameters cannot be avoided. However, the two-step algorithm presented here makes a simultaneous reconstruction feasible.

The modifications to the algorithm required prior to its application in the reconstruction of clinical data, namely the incorporation of non-scattering regions, and the extension to a fully three-dimensional model, are currently being carried out by our group.

### Acknowledgment

This work was supported by the Wellcome Trust.

### References

- Arridge S R 1995 Photon measurement density functions. Part 1: analytical forms *Appl. Opt.* **34** 7395–409
- 1999 Optical tomography in medical imaging *Inverse Problems* **15** R41–R93
- Arridge S R and Schweiger M 1995a Direct calculation of the moments of the distribution of photon time of flight in tissue with a finite-element method *Appl. Opt.* **34** 2683–7
- 1995b Photon measurement density functions. Part 2: finite element calculations *Appl. Opt.* **34** 8026–37
- 1995c Sensitivity to prior knowledge in optical tomographic reconstruction *Proc. SPIE* **2389** 378–88
- 1995d Reconstruction in optical tomography using MRI based prior knowledge *Information Processing in Medical Imaging '95* ed Y Bizais, C Barillot and R di Paola (Heidelberg: Springer) pp 77–88
- 1998 A gradient-based optimisation scheme for optical tomography *Opt. Express* **2** 213–26. <http://www.epubs.osa.org/oearchive/source/4014.htm>
- 1999 A general framework for iterative reconstruction algorithms in optical tomography, using a finite element method *Computational Radiology and Imaging: Therapy and Diagnosis (IMA Volumes in Mathematics and its Applications 110)* ed C Borgers and F Natterer (New York: Springer) pp 45–70
- Arridge S R, Dehghani H, Schweiger M and Okada E 1999 The finite element model for the propagation of light in scattering media: a direct method for domains with non-scattering regions *Med. Phys.* at press
- Arridge S R, Hiraoka M and Schweiger M 1995 Statistical basis for the determination of optical pathlength in tissue *Phys. Med. Biol.* **40** 1539–58
- Arridge S R, Schweiger M, Hiraoka M and Delpy D T 1993 A finite element approach for modeling photon transport in tissue *Med. Phys.* **20** 299–309
- Benaron D A, Van Houten J P, Cheong W-F, Kermit E L and King R A 1995 Early clinical results of time-of-flight optical tomography in a neonatal intensive care unit *Proc. SPIE* **2389** 582–9
- Chang J, Graber H L, Koo P C, Aronson R, Barbour S-L and Barbour R L 1997 Optical imaging of anatomical maps derived from magnetic resonance imaging using time-independent optical sources *IEEE Trans. Med. Imaging* **16** 68–77
- Chen C-T, Ouyang X, Wong W H, Hu X, Johnson V E, Ordonez C and Metz C E 1991 Sensor fusion in image reconstruction *IEEE Trans. Nuclear Science* **38** 687–92
- Fantini S, Franceschini M A, Gaida G, Gratton E, Jess H, Mantulin W W, Moesta K T, Schlag P M and Kaschke M 1996 Frequency-domain optical mammography: edge effect corrections *Med. Phys.* **23** 149–57
- Firbank M, Arridge S R, Schweiger M and Delpy D T 1996 An investigation of light transport through scattering bodies with non-scattering regions *Phys. Med. Biol.* **41** 767–83
- Firbank M, Hiraoka M, Essenpreis M and Delpy D T 1993 Measurement of the optical properties of the skull in the wavelength range 650–950 nm *Phys. Med. Biol.* **38** 503–10
- Gindi G, Lee M, Rangarajan A and Zubal I G 1993 Bayesian reconstruction of functional images using anatomical information as priors *IEEE Trans. Med. Imaging* **12** 670–80
- Gratton G, Corballis P M, Cho E, Fabiani M and Hood D C 1995 Shades of gray matter: noninvasive optical images of human brain responses during visual stimulation *Psychophysiology* **32** 505–9
- Hielscher A H, Klose A D and Hanson K M 1999 Gradient-based iterative image reconstruction scheme for time-resolved optical tomography *IEEE Trans. Med. Imaging* **18** 262–71
- Hoshi Y and Tamura M 1993 Dynamic multichannel near-infrared optical imaging of human brain activity *J. Appl. Phys.* **75** 1842–6

- Maki A, Yamashita Y, Ito Y, Watanabe E, Mayanagi Y and Koizumi H 1995 Spatial and temporal analysis of human motor activity using noninvasive NIR topography *Med. Phys.* **22** 1997–2005
- Leahy R and Yan X 1991 Incorporation of anatomical MR data for improved functional imaging with PET *Information Processing in Medical Imaging (IPMI'91 Proc.) (Lecture Notes in Computer Science 511)* (Heidelberg: Springer) pp 105–20
- Moesta K T, Fantini S, Jess H, Totkas S, Franceschini M A, Kaschke M and Schag P M 1998 Contrast features of breast cancer in frequency-domain laser scanning mammography *J. Biomed. Opt.* **3** 129–36
- Model R, Orlt M, Walzel M and Hünlich R 1997 Reconstruction algorithm for near-infrared imaging in turbid media by means of time-domain data *Appl. Opt.* **14** 313–24
- Okada E, Firbank M, Schweiger M, Arridge S R, Cope M and Delpy D T 1997 Theoretical and experimental investigation of near-infrared light propagation in a model of the adult head *Appl. Opt.* **36** 21–31
- Paulsen K D and Jiang H 1995 Spatially-varying optical property reconstruction using a finite element diffusion equation approximation *Med. Phys.* **22** 691–701
- Paulsen K D, Meaney P M, Moskowitz M J and Sullivan J M Jr 1995 A dual mesh scheme for finite element based reconstruction algorithms *IEEE Trans. Med. Imaging* **14** 504–14
- Pogue B W and Paulsen K D 1998 High-resolution near-infrared tomographic imaging simulations of the rat cranium by use of *a priori* magnetic resonance imaging structural information *Opt. Lett.* **23** 1716–18
- Saquist S S, Hanson K M and Cunningham G S 1997 Model-based image reconstruction from time-resolved diffusion data *Proc. SPIE* **3034** 369–80
- Schweiger M and Arridge S R 1997a The finite element method for the propagation of light in scattering media: frequency domain case *Med. Phys.* **24** 895–902
- 1997b Optimal data types in optical tomography *Information Processing in Medical Imaging (IPMI'97 Proc.) (Lecture Notes in Computer Science 1230)* (Heidelberg: Springer) pp 71–84
- 1997c Direct calculation with a finite-element method of the Laplace transform of the distribution of photon time of flight in tissue *Appl. Opt.* **36** 9042–9
- 1998 Comparison of 2D and 3D reconstruction methods in optical tomography *Appl. Opt.* **37** 7419–28
- 1999 Application of temporal filters to time-resolved data in optical tomography *Phys. Med. Biol.* **44** 1699–717
- Schweiger M, Arridge S R and Delpy D T 1993 Application of the finite-element method for the forward and inverse models in optical tomography *J. Math. Imaging Vision* **3** 263–83
- Schweiger M, Arridge S R, Hiraoka M and Delpy D T 1995 The finite element model for the propagation of light in scattering media: boundary and source conditions *Med. Phys.* **22** 1779–92
- van der Zee P 1993 Measurement and modelling of the optical properties of human tissue in the near infrared *PhD Thesis* University of London
- Wyatt J S, Cope M, Delpy D T, Richardson C E, Edwards A D, Wray S C and Reynolds E O R 1990 Quantitation of cerebral blood volume in newborn infants by near infrared spectroscopy *J. Appl. Phys.* **68** 1086–91
- Zhou S, Xie C, Nioka S, Liu H, Zhang Y and Chance B 1997 Phased array instrumentation appropriate to high-precision detection and localization of breast tumor *Proc. SPIE* **2979** 98–106